




Article

Rutile from Panasqueira (Central Portugal): An Excellent Pathfinder for Wolframite Deposition

Eleonora Carocci ¹, Christian Marignac ^{2,*} , Michel Cathelineau ^{1,*} , Laurent Truche ³, Andrei Lecomte ¹ and Filipe Pinto ^{4,5} 

¹ GeoRessources, Université de Lorraine, CREGU, rue Jacques Callot, F-54506 Vandoeuvre-lès-Nancy, France; eleonora.carocci@univ-lorraine.fr (E.C.); andrei.lecomte@univ-lorraine.fr (A.L.)

² GeoRessources, Université de Lorraine, Ecole Nationale Supérieure des Mines de Nancy, Parc de Saurupt, F-54042 Nancy, France

³ ISTERRE, Université de Grenoble-Alpes, F-38041 Grenoble, France; laurent.truche@univ-grenoble-alpes.fr

⁴ Beral Tin and Wolfram Portugal, 6225-051 Barroca Grande, Portugal; filipe.pinto@beraltportugal.pt

⁵ Instituto de Ciências da Terra, Rua Campo Alegre 687, 4169-007 Porto, Portugal

* Correspondence: christian.marignac@univ-lorraine.fr (C.M.); michel.cathelineau@univ-lorraine.fr (M.C.); Tel.: +33-679-213-617 (C.M.); +33-372-745-543 (M.C.)

Received: 31 October 2018; Accepted: 18 December 2018; Published: 24 December 2018



Abstract: Abundant W-rich rutile in the tourmalinized wall-rocks from the Panasqueira W-deposit appears to be a marker of the onset of the main wolframite depositing event. Rutile displays spectacular zoning, both sector (SZ) and oscillatory (OZ). An extensive set of compositional data obtained on crystals, beforehand studied using back-scattered electron images and X-ray maps, was used to address (i) the effects of SZ on differential trapping of minor elements, and (ii) the significance of the OZ in deciphering fluid sources and fluid circulation dynamics. Particular attention was paid to Sn, W (Nb, Ta) concentrations in rutile as pathfinders of the W deposition. Concerning the sector zoning, W is more incorporated than (Nb, Ta) onto more efficient faces, whereas Sn contents are nearly not impacted. The net effect of the sector zoning is thus a progressive increase of the relative weight of Sn from pyramid to prism faces, in combination with a less significant increase in the relative weight of Nb + Ta. The oscillatory zoning concerns most minor elements: W, Nb (Ta), Fe, V, Cr and Sn. In the frequent doublets, the clear bands are in general enriched in W relatively to the dark ones, whereas the inverse is true for Nb and Ta. The doublets may be viewed as the result of the successive influx of (i) a W-rich, Nb + Ta poor fluid, abruptly replaced by (or mixed to) (ii) a Nb + Ta-rich and W-poor fluid. The Nb + Ta-rich fluid could be in turn related to a rare-metal granite layer observed atop of the Panasqueira granite.

Keywords: W-rich Rutile; sector zoning; oscillatory zoning; fluid source signature; wolframite; Panasqueira

1. Introduction

Rutile is the most abundant Ti-bearing mineral and a very common accessory mineral stable in a wide range of geological environments from igneous to sedimentary settings [1]. Rutile may incorporate a variety of elements, and in particular Al, V, Cr, Fe, Zr, Nb, Sn, Sb, Hf, Ta, W and U [2–10]. Trace elements in rutile may be used as marker of sediment sources, e.g., [11,12], or to probe subduction and magmatic processes, e.g., [1,13–15]. Rutile is also widely used to date (U/Pb) metamorphic events [1,16], and references therein, less commonly magmatic events, e.g., [17], or ore deposition, e.g., [18–21]. Zr content in rutile may also be used as a geo-thermometer [22].

Rutile is common in felsic magmatic rocks, and an extensive literature deals with Nb and Ta-bearing rutile in rare-metal granites and pegmatites as a marker of magmatic processes such

as fractionation or mixing, e.g., [23–31]. Rutile is also found in a variety of ore deposit types, including orogenic gold, porphyry copper [32], VHMS (Volcanic-Hosted Massive Sulfide), skarns, and hydrothermal W–Sn veins [33]. HFSE (High Field Strength Elements) spectra in rutile may be used to discriminate different stages of ore deposition or different types of deposits [33].

W-rich rutile (i.e., rutile with ≥ 1 wt % W) is comparatively rare, and is mainly found in epithermal deposits [6], orogenic gold deposits [34–36], rare metal pegmatites [37], and W-bearing deposits, e.g., [33,38]. In such occurrences, W content in rutile may be as high as, for instance: 7.2 wt % in a Mo-bearing aplite [39]; 8 wt % in some W-skarn deposits [40]; 9.5 wt % in orogenic gold deposit of Kalgoorlie [36]; 9.6 wt % at Puy-Les-Vignes (W-deposit) [38]. Rutile is also known to display zoning textures, most commonly sector zoning, e.g., [6], but also oscillatory zoning, e.g., [10]. Yet, detailed studies of rutile zoning aimed to interpretation of the rutile growth environment are surprisingly rare.

In this paper, we explore W-rich rutile from the Panasqueira W–Sn–Cu deposit (Central Portugal), that is found to be abundant accessory phase in tourmalinized wall-rock. Both tourmaline and rutile are involved at the main wolframite depositing event [21] which has made Panasqueira one of the largest W deposit in Western Europe. This W-rich rutile displays spectacular zoning, both sector (SZ) and oscillatory (OZ). We use an extensive set of composition data to address (i) the differential trapping of minor elements in SZ, and (ii) the significance of the OZ in terms of fluid sources and fluid circulation dynamics. Particular attention was paid to Sn, W (Nb, Ta) concentrations in rutile as the latter may be considered as a pathfinder of the W deposition.

2. Geological Setting

Panasqueira is located in the Variscan Central Iberian Zone (CIZ) (Figure 1B). The Panasqueira W–Sn–Cu mine, active more than 100 years, was for long one of the largest tungsten deposits in Western Europe, amounting for at least c. 111 kt W (the sum of a past production of at least 88 kt-W in 1947–2014 [41], and of remaining reserves + resources of ~ 23 kt W [42]), and thus contributing for more than one third to the CIZ tungsten endowment. The deposit is hosted in greenschist facies micaschists belonging to the Beira Schists Complex [43] and consists of a swarm of sub-horizontal W–Sn–Cu bearing quartz veins extending for over 10 km² with a vertical extent of around 300 m (Figure 1A). A large concealed granite body with a laccolith shape [44] is associated with a metamorphic contact spotted aureole, crosscut by the vein swarm. Atop of this body, layers and a cupola of rare metal granites [45–47] are more or less affected by greisenization and also overprinted by the vein system. This deposit has been the subject of many studies, e.g., [45,46,48–65]. The deposit experienced a protracted history, beginning with a strong tourmalinization of the wall-rocks [63,65], heralding the main wolframite deposition event. Rutiles are systematically associated with tourmaline and are dated using U–Pb method at 305.2 ± 5.7 Ma [65].

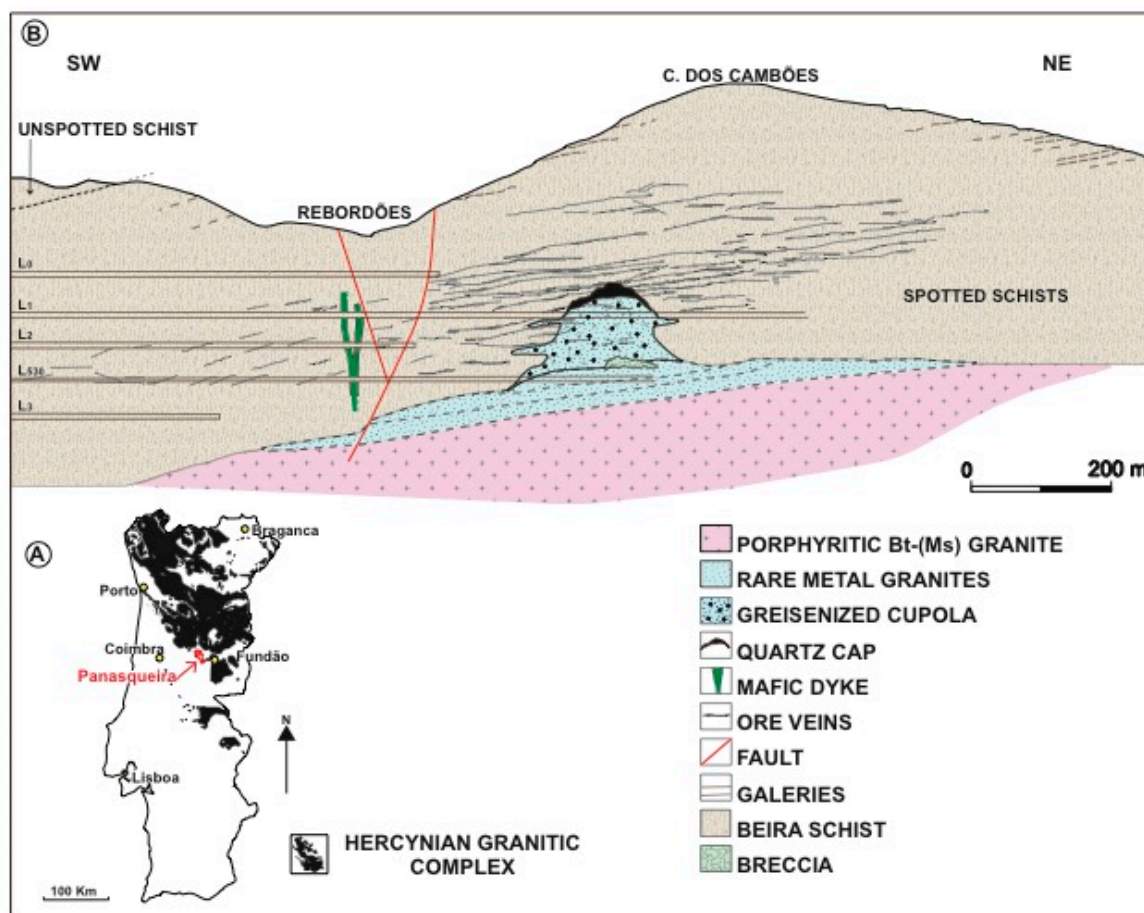


Figure 1. (A) Distribution of Hercynian granitic rocks and the Panasqueira location (modified after [45]). (B) Schematic cross section of the Panasqueira deposit, showing the concealed granites and greisenized cupola with a silica cap, and the gently dipping quartz–wolframite vein system (modified after [46,47]).

3. Material and Methods

Classical petrographic examinations have been carried out using an Olympus BX51 (transmitted and reflected light) optical microscope and a VHX-200 Keyence numeric microscope. Selected polished thin sections were studied with a JEOL J7600F scanning electron microscope (SEM) equipped with a Silicon Drift Detector (SDD)-type EDS spectrometer at the GeoRessources Laboratory (Nancy, France). Backscattered electron (BSE) images were obtained by setting the acceleration voltage at 15 kV. X-ray mapping was done using a CAMECA SX100 Electron microprobe (EPMA) equipped with a wavelength dispersive spectrometer (WDS), with a 12 nA current and an accelerating voltage of 15 kV. Micro-XRF mapping was done using the Bruker-Nano M4 Tornado instrument. This system has a Rh X-ray tube with a Be side window and polycapillary optics giving an x-ray beam with a diameter of 25–30 μm on the sample. The X-ray tube was operated at 50 kV and 200 μA . X-rays are detected by a 30 mm² XFlash®SDD with an energy resolution of <135 eV at 250,000 cps. All analyses were carried out at 2 kPa vacuum. Main elements such as Fe, Ti, Cl, Al, and Si were mapped, and composite images were generated. Major-element mineral compositions were determined using a JEOL J7600F SEM at the GeoRessources Laboratory (Nancy, France). Analytical conditions were a 1 nA current and an acceleration voltage of 15 kV, with a counting time of 60 s. Natural and synthetic oxides and silicate standards were used: MnTiO₃ (Ti), Cr₂O₃ (Cr), vanadinite (V), hematite (Fe), LiNbO₃ (Nb), LiTaO₃ (Ta), cassiterite (Sn) and scheelite (W). Detection levels were taken at ~1000 ppm for all elements, except Ta. Due to overlap with the W peak, Ta detection level is set at ~3000 ppm. However, in many cases,

although a clear shouldering on the W peak testifies for the presence of Ta, disentangling is not feasible. In such instances, we arbitrarily set a Ta value at 1500 ppm, i.e., at the best estimate without bias.

4. Results

4.1. Petrography

Rutile crystals are found either scattered or densely disseminated in the tourmalinized wall rocks, or associated with tourmaline in thin early quartz veinlets (Qcs) resulting from a crack-seal process [58] (Figure 2A,B). In the wall rocks, they occur either as single crystals (Figure 3C,D) or aggregates (Figure 3B), sometimes chain of crystals, with a size from less than 10 μm up to 80–100 μm , varying from sample to sample. They locally may be associated with zircon or Th-rich monazite. In the Qcs veinlets, they form isolated larger crystals (Figure 3E,F), up to 500 μm or more in diameter. Rutile crystals commonly contain euhedral quartz or muscovite inclusions.

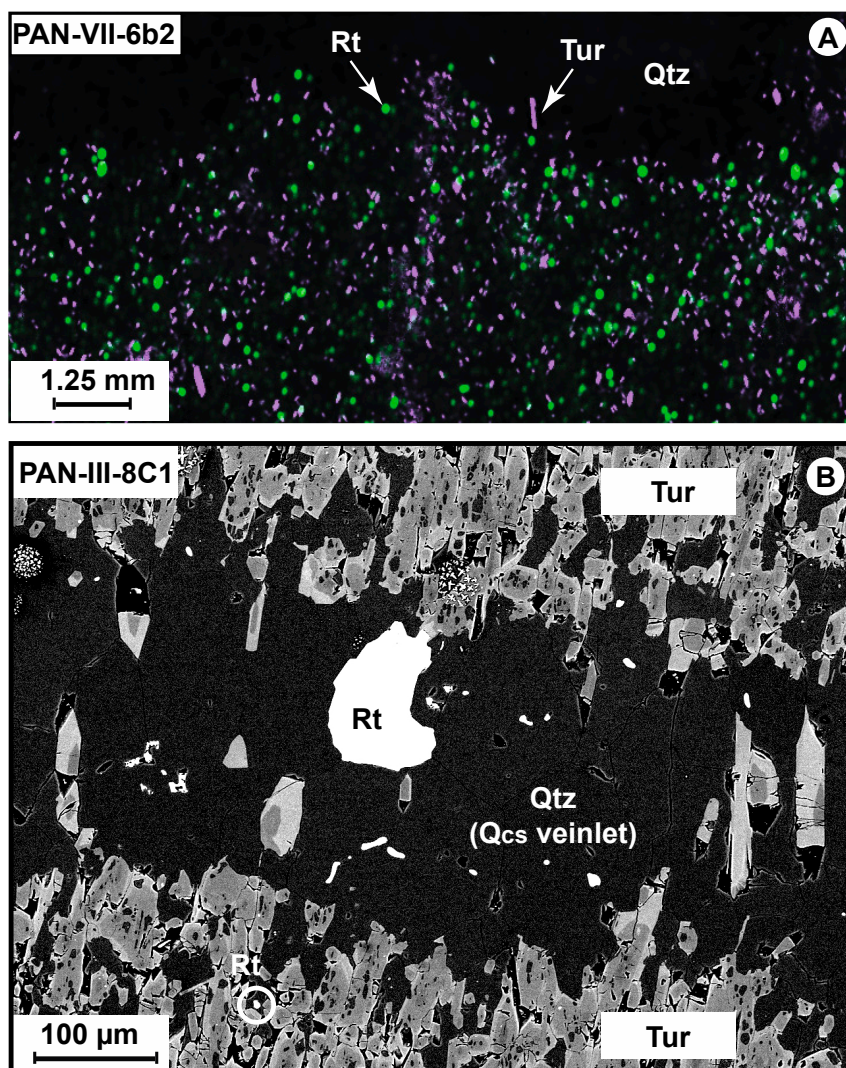


Figure 2. (A) A false-colored μ -XRF composite map of the wall rock from a wolframite-bearing quartz vein. Tourmaline (Tur) is imaged by Cl and rutile (Rt) by Ti, Qtz = quartz. (B) BSE image of an early quartz veinlet (Qcs) bearing rutile. Tourmalinization in the wall rock is coeval with the Qcs, as shown by the tourmaline crystals protruding into the veinlet.

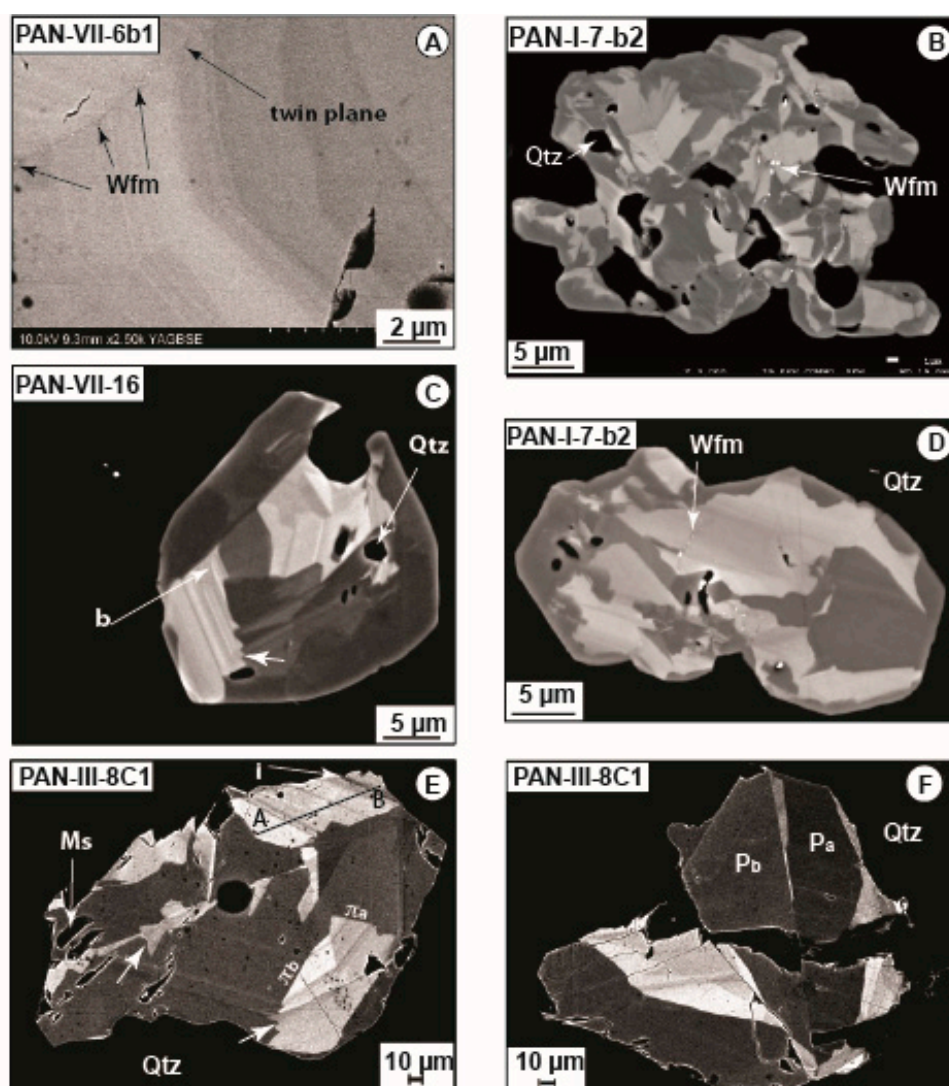


Figure 3. Aspects of the Panasqueira rutile crystals (SEM-BSE). Note the ubiquitous sector zoning, marked by the strong contrast in BSE images, and the well-expressed oscillatory zoning (OS), particularly in metal-rich pyramidal sectors (A, F–G crystals from Qcs veinlets, B–D crystals from tourmalinized wall rock). (A) Location of wolframite nano-inclusions along a twin plane. (B) Aggregate of crystals, with abundant wolframite (Wfm) as nano-inclusions. (C) Small isometric crystal; note the “fir-tree” texture (arrow) typical of the sector zoning, and the beveling (b) in the OS. (D) Composite crystal, rich in wolframite (Wfm) nano-inclusions; note the “fir-tree” texture (arrow). (E) Particularly well-expressed oscillatory zoning in a large crystal; note the inversion in the OS trends in i, and the “fir-tree” texture (arrows); π_a and π_b , two types of pyramid faces (see text for definition); Ms muscovite; A–B: profile in Figure 10. (F) Twinned crystal; Pa and Pb, two types of prism faces (see text for definition).

Micro- to nano-inclusions (1–100 nm) of zircon or wolframite are not rare, and up to 10 or more nano-crystals may be contained in a single crystal. Wolframite nano-inclusions are usually located at crystallographic boundaries (such as faces intersections, twin planes, and quartz inclusion boundary) (Figure 3A,B,D), suggesting that their growth was coeval with the host rutile. Compositions estimated from SEM-EDS are ferberitic, with a Fe/Fe + Mn ratio between 0.67 and 0.83. From detailed relationships between rutile, tourmaline and early wolframite, it is inferred that rutile deposition was coeval with the inception of the main wolframite depositing event [21].

4.2. Rutile Chemical Composition

The crystals are typically zoned on a scale of the order of 10 μm or less, precluding measurement of their chemical composition by EPMA. For this reason, the chemical composition was measured (including oxygen) by SEM-EDS on the basis of the back-scattered images. Sixty-one crystals from 12 samples were studied in great detail, and a selection of results is presented in Table 1 (the whole set of data is provided in Supplementary Data Table S1). Structural formulae were calculated on a 3 cation basis, to conform to the general formula AB_2O_6 . With an average 6.04 apfu (Atom Per Formula Unit) the calculated structural O is found to be very close to 6, attesting to the good quality of the analyses. The Panasqueira rutile systematically contains Fe, V, Sn, Nb, Ta and W, all with highly variable contents, in part because of sector zoning effects (see below): Fe from 0.18 to 2.95 wt %, V from below detection level (bdl) to 3.48 wt %, Cr from bdl to 2.41 wt %, Nb from bdl to 1.64 wt %, Ta from bdl to 2.17 wt %, and W from 0.20 to 9.45 wt %. Nb + Ta is usually lower than 0.5 wt %, and the Nb/Nb + Ta ratio varies from 0.05 to 0.97, being on average 0.6.

Table 1. Selected EDS analyses of different faces of rutile crystals.

Qcs Veinlet						Wall Rock					
Crystal Face	A Pa	A Pb	A π a	A π b	A π b	B Pa	C Pb	D π a	E π a	F π b	G π b
W	0.99	1.75	3.92	5.01	9.13	0.33	1.64	2.59	4.37	5.97	6.37
Sn	0.51	0.62	0.75	0.45	0.71	0.67	0.75	0.84	0.95	1.66	0.79
Nb	1.24	0.16	0.21	0.26	0.22	0.23	0.12	0.16	0.21	1.48	bdl
Ta	0.15	0.34	0.15	0.15	0.15	0.43	0.36	0.32	0.15	0.58	0.33
Cr	bdl	bdl	0.27	0.15	1.39	bdl	0.18	bdl	1.56	bdl	bdl
V	0.58	0.5	0.96	0.74	0.66	0.19	0.67	0.56	0.55	0.60	0.56
Fe	0.59	0.58	0.96	1.29	1.40	0.42	0.36	0.95	0.20	2.05	1.91
Ti	56.22	57.28	54.11	53.46	50.08	58.24	57.09	55.75	53.28	50.72	51.85
O	39.28	39.68	38.79	38.5	37.92	39.70	39.67	39.13	38.39	38.00	37.85
Σ	99.65	100.91	100.12	100.01	101.66	100.21	100.84	100.30	99.80	101.06	99.67
Base 3 Cations											
W	0.013	0.023	0.053	0.069	0.127	0.004	0.022	0.035	0.060	0.083	0.089
Sn	0.011	0.013	0.016	0.010	0.015	0.014	0.015	0.017	0.020	0.036	0.017
Nb	0.033	0.004	0.006	0.007	0.006	0.006	0.003	0.004	0.006	0.41	
Ta	0.003	0.005	0.002	0.003	0.002	0.006	0.005	0.004	0.003	0.008	0.005
Cr			0.013	0.007	0.069		0.008	0.000	0.075		
V	0.028	0.024	0.047	0.037	0.033	0.009	0.032	0.027	0.027	0.030	0.028
Fe	0.026	0.025	0.043	0.058	0.064	0.018	0.016	0.042	0.009	0.094	0.088
Ti	2.882	2.906	2.820	2.810	2.683	2.943	2.899	2.870	2.799	2.708	2.773
O	6.025	6.023	6.049	6.054	6.078	6.002	6.026	6.027	6.035	6.071	6.057
Nb + Ta	0.04	0.01	0.01	0.02	0.01	0.01	0.01	0.01	0.01	0.05	0.01
Nb#	0.92	0.43	0.72	0.74	0.75	0.51	0.39	0.49	0.630	0.83	0

For labeling of faces, see text; bdl below detection level; for Ta, 0.15 is set as the best estimate value when disentangling from the W peak was not feasible (see chapter “Methods”). A: sample PAN-VII-6-b1; B: sample PAN-II-10a; C: sample PAN-IV-5; D: sample PAN-IV-3b; E: sample PAN-VII-16; F: sample PAN-XIII-6-c2; G: sample PAN-IV-5.

The crystals display a marked sector zoning, often combined with typical oscillatory zoning (Figure 3). All the minor elements, W, Nb (Ta), Fe, V, Cr and Sn, are equally involved in the zoning (Figure 4). Sector zoning is exhibited mostly by W and Fe, a fact already mentioned by [6], and, although to a lesser extent, by Nb and Ta (Figure 4B,F–K), whereas Sn, V (and Cr) are less systematically affected: compare Sn or V in Figure 4D–H, and Figure 4J–M.

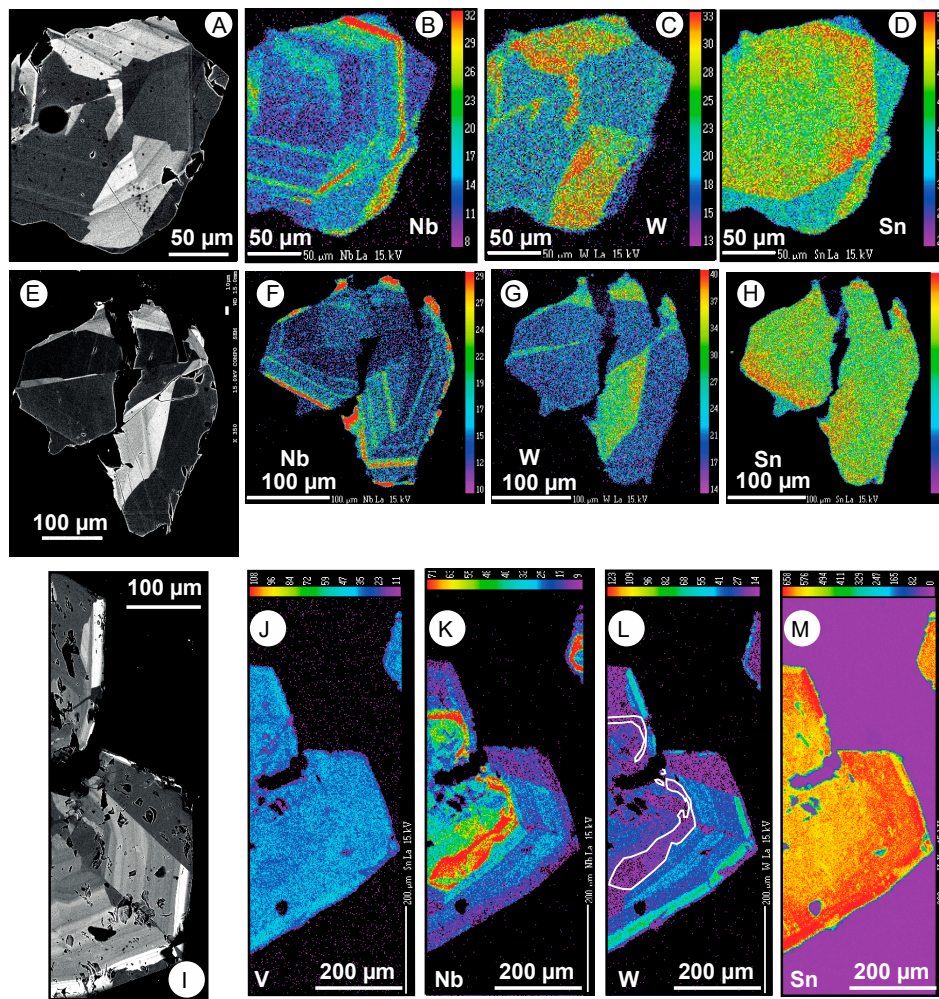
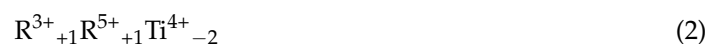


Figure 4. Characterization of the zoning in Panasqueira rutiles by coupling BSE images and false-color coded X-ray (EPMA) maps. Warmer colors correspond to higher concentrations. All crystals are from Qcs veinlets. Note the combination of conspicuous sector and oscillatory zoning. (A–D): a crystal from sample PAN-III-8-c1. (A) BSE image, (B–D) X-ray maps. (E–H): a twinned crystal from the same sample. (E) BSE image, (F–H) X-ray maps. (I–M): part of a very large crystal from sample PAN-VII-6-b1. (I) BSE image, (J–M) X-ray maps; in (L) white lines underline the areas with the highest Nb concentrations in (K).

5. Interpretation

5.1. Crystal Chemistry

In the general AB_2O_6 structure, in which TiO_2 may be seen as an end-member, entrance of W^{6+} or $R(Nb, Ta)^{5+}$ is generally thought to be due to coupling with a R^{3+} cation, according to the exchange vectors:



Exchange between W^{6+} and R^{5+} is also possible, equally involving coupling with a R^{3+} cation, according to:



The R^{3+} cation could be Al^{3+} , not documented at Panasqueira, and Cr^{3+} , V^{3+} or Fe^{3+} .

Iron is commonly thought to enter the rutile structure as Fe^{3+} , e.g., [66], but Fe^{2+} is sometimes considered [37], entering the structure according to the vectors:

$$\text{Fe}^{2+}_{+1}\text{W}^{6+}_{+1}\text{Ti}^{4+}_{-2} \quad (4)$$

$$\text{Fe}^{2+}_{+1}\text{R}^{5+}_{+2}\text{Ti}^{4+}_{-3} \quad (5)$$

Tin (Sn^{4+}) directly replaces Ti. Among the three possible V valences, V^{4+} is the more prone to replacing Ti, followed by V^{3+} and then V^{5+} , according to [67]. V^{4+} will directly replace Ti, and V^{5+} will exchange with R^{5+} .

The valences of Fe and V in the rutile structure may be discriminated according to the following considerations. When all vectors are considered, and both Fe^{2+} and Fe^{3+} are supposed to be present, the following relationship is valid (in apfu):

$$2\text{Fe}^{2+} + (2a + b - c) + \text{Cr} + \text{V}^{3+} = 2\text{W} + \text{Nb} + \text{Ta} \quad (6)$$

where all V is considered V^{3+} and a, b, and c are respective coefficients (between 0 and 1) of the vectors (1), (2) and (3) where $\text{R}^{3+} = \text{Fe}^{3+}$. With $\text{Fe}^{2+} = X$ and consequently $\text{Fe}^{3+} = 1 - X$ (i.e., $2a + b - c = 1 - X$), Equation (6) reduces to:

$$X + 1 = 2\text{W} + \text{Nb} + \text{Ta} \quad (7)$$

It follows that in a Fe + Cr + V vs. $2\text{W} + \text{Nb} + \text{Ta}$ diagram, when all V is considered to be V^{3+} , all the rutile analyses should plot between two lines corresponding to two extreme cases:

$$2\text{Fe}^{2+} + \text{Cr} + \text{V} = 2\text{W} + \text{Nb} + \text{Ta} \quad (\text{all Fe as Fe}^{2+}) \quad (8)$$

$$\text{Fe}^{3+} + \text{Cr} + \text{V} = 2\text{W} + \text{Nb} + \text{Ta} \quad (\text{all Fe as Fe}^{3+}) \quad (9)$$

Thus, theoretically allowing a qualitative evaluation of the Fe^{2+} to Fe^{3+} proportion. In the Panasqueira case, owing to the fact that as a rule $2\text{W} \gg \text{Nb} + \text{Ta}$, the slopes of lines (8) and (9) will be close to 1 and 0.5, respectively. If, nevertheless, other V valences are involved, they will be expressed by shifts of the plotted analyses in the preceding diagram, i.e., vertically if V^{4+} is present, and horizontally if V^{5+} is present. If the analyses plot above line (8), the involvement of V^{4+} is likely, and in the same way, if they plot below line (9), the presence of V^{5+} may be envisaged. However, if they plot in between the two lines (8) and (9), the effects of valence changes in Fe and V will be indiscernible.

Nevertheless, replacing Fe + Cr + V by Fe + Cr in the testing diagram may allow an independent evaluation of the possible effect of the V^{3+} to V^{4+} shift. As seen in Figure 5A, when plotted in the Fe + Cr + V (apfu) vs. $2\text{W} + \text{Nb} + \text{Ta}$ (apfu) diagram (i.e., assuming all V as V^{3+}), the Panasqueira rutile crystals predominantly occupy the whole interval between the two (8) and (9) lines, with a neat tendency to overlap the “ V^{4+} domain” and with trends which are not rooted at zero. By contrast, when plotted in the Fe + Cr (apfu) vs. $2\text{W} + \text{Nb} + \text{Ta}$ (apfu) diagram (i.e., assuming all V as V^{4+}), the Panasqueira rutile crystals are in their great majority on (or close to) the (9) line (Figure 5B). This behavior is readily explained if in the crystals (i) Fe is predominantly present as Fe^{3+} , and (ii) concomitantly V is predominantly present as V^{4+} . In a few occurrences, however, distinct shifts from the (9) line are still present in the diagram of Figure 5B. In one case (sample II-10a), vertical shifts may be interpreted as recording the presence of Fe-rich nano-inclusions, most likely, ilmenite. In sample XIII-1c, most analyses are under the (9) line, meaning that in this sample, a higher proportion of vanadium is present as V^{3+} .

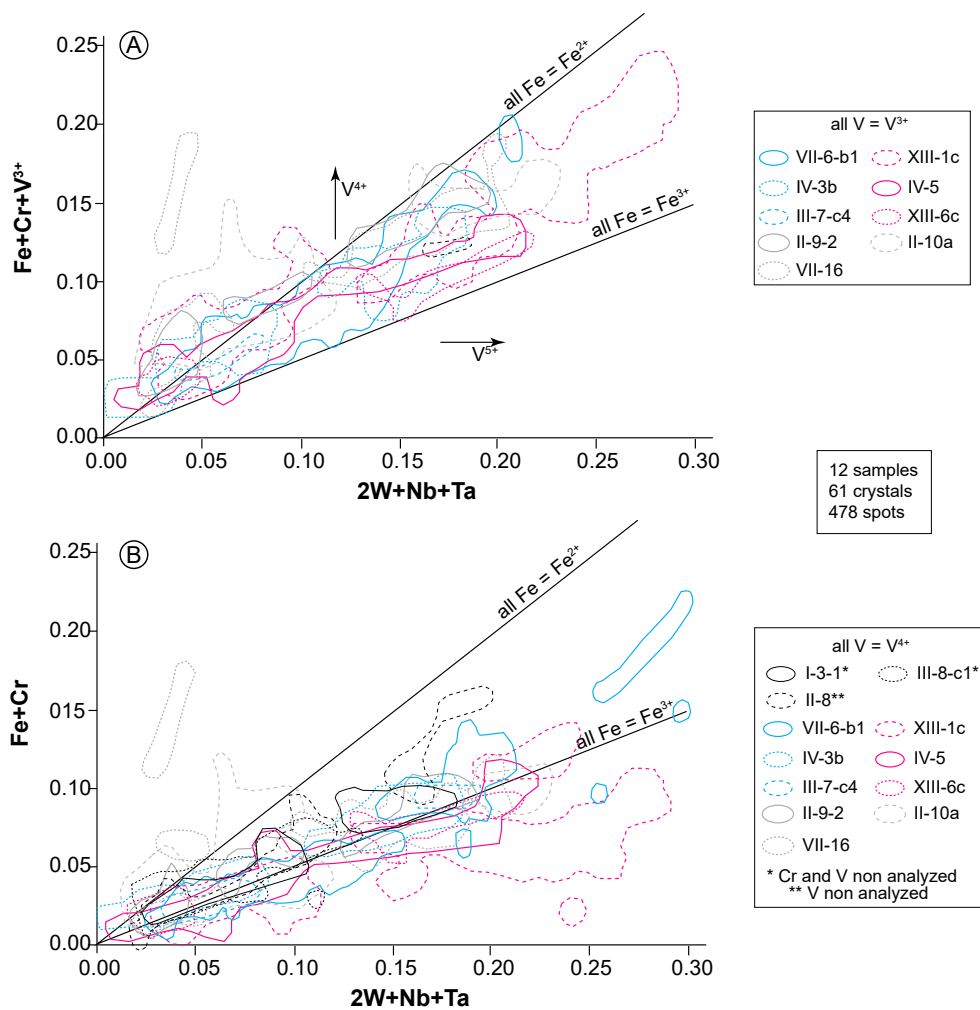


Figure 5. Unravelling Fe and V valences in the Panasqueira rutile: plot of trivalent cations vs. 2W + Nb + Ta. (A). All V is assumed to be present as V³⁺. (B) All V is assumed to be present as V⁴⁺. When present in a sample, outliers are drawn as isolated from the main field for this sample. Explanations in the text.

5.2. Compositional Zoning: Sector Zoning

Patterns of sector zoning are said to be “a function of both crystal habit and how it changes with progressive growth”, commonly leading to typical “fir-tree” shaped sectors [68]. BSE images of rutile sections may therefore be complicated and difficult to interpret, in particular, where crystals are aggregated, which is a common case at Panasqueira (e.g., Figure 3B). On favorable sections, seemingly close to being parallel, or orthogonal, to the prism axis, comparison of BSE images with ideal rutile form shows that we are apparently dealing with two tetragonal prisms ($a = \{100\}$ and $m = \{110\}$) and two dipyrramids ($e = \{101\}$, and $s = \{111\}$) (Figure 6). It appears that the crystal sectors that more efficiently concentrate metals are associated with pyramid faces (Figure 6). This is at variance with the opinion of [6], who thought that this role was taken by the prism faces in the W-rich rutile crystals at Kori Kollo gold mine (Bolivia). It also appears that the two sets of prisms or the two sets of pyramids are not equivalent, one of them being systematically more efficient in concentrating minor elements than the other, as seen by the contrasting grey hues in BSE images (Figure 6). Unfortunately, it was not possible to properly index the faces, and consequently we choose to label π_a and π_b the two sets of tetragonal pyramid faces, with π_b the more efficient, and P_a and P_b the two sets of tetragonal prism faces, with P_b the more efficient (Figure 6). The different forms are variably combined, with apparently

all the possibilities between prism-dominated or pyramid-dominated habits, nearly isometric habits being seemingly the more common. Otherwise, P_a and π_b are by far the most common faces.

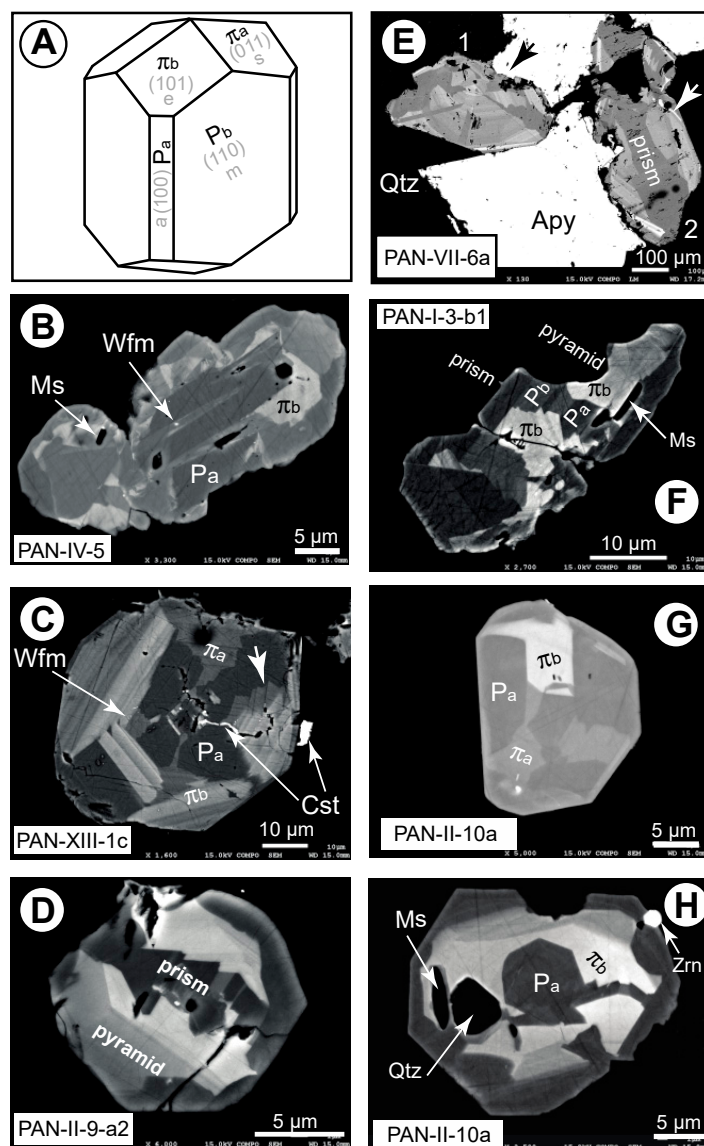


Figure 6. Interpretative identification of the crystallographic faces involved in the sector zoning (SEM-BSE). Prism faces: P_a and P_b ; pyramid faces: π_a and π_b (see text for definitions). All crystals are from tourmalinized wall rock, except D, taken from a Qcs veinlet. (A) Theoretical rutile crystal combining two tetragonal prisms (a and m) and two tetragonal dipyrramids (e and s). In the figure is also shown one of the two possible connections between the indexed crystallographic faces and the P_a , P_b , π_a , π_b notation. (B) Crystal with a prismatic habitus; Ms muscovite, Wfm wolframite. (C) Section near to perpendicular to A4 axis. Sector zoning is well defined, with typical "fir-tree" texture (arrow). Note the contrast between the syn-rutile growth wolframite (Wfm) nano-inclusions, located at the OS boundaries, and the cassiterite (Cst), post-dating rutile growth. (D) Isometric crystal, seemingly showing a greater development of the pyramid faces. (E) Two large crystals displaying a morphology controlled by the dipyrramids, with a flattened prism: crystal 1 would be cut near to perpendicular, and crystal 2, near to parallel, to the A4 axis. Both crystals are earlier than the arsenopyrite (Apy) (corrosion: arrows). (F) The two types of prism face are well discriminated in a section oblique onto the A4 axis; Ms muscovite. (G) The two types of pyramid face are well identified. (H) Example of a nondescript section in which face identification is not easy and may remain subjective; Ms muscovite, Zrn zircon.

Quantitatively, systematic measurement of rutile composition as a function of the face shows that W and Fe are preferentially concentrated in the pyramid faces, as do Nb and Ta in a lesser proportion, whereas V, (Cr) and Sn are almost not affected by the differential trapping (Table 1). The maximum W concentration in a given type of face is variable, depending on the samples: 1.12 to 10.7 wt % in π_b , 1.07 to 7.62 wt % in π_a , 0.64 to 3.92 wt % in P_b and 0.26 to 1.40 wt % in P_a . In π_b and π_a , the Panasqueira rutile appears as one of the richest in W worldwide. The partitioning of the four types of faces is well displayed in the W–Sn–(Nb + Ta) diagram in Figure 7. As seen in Figure 7, W is more incorporated than Nb and Ta onto the more efficient faces, whereas Sn contents are nearly not impacted. As a consequence, the net effect of the sector zoning is a progressive increase of the relative weight of Sn from π_b to π_a then to P_b and finally to P_a . This effect combines with a less significant increase of the relative weight of Nb + Ta.

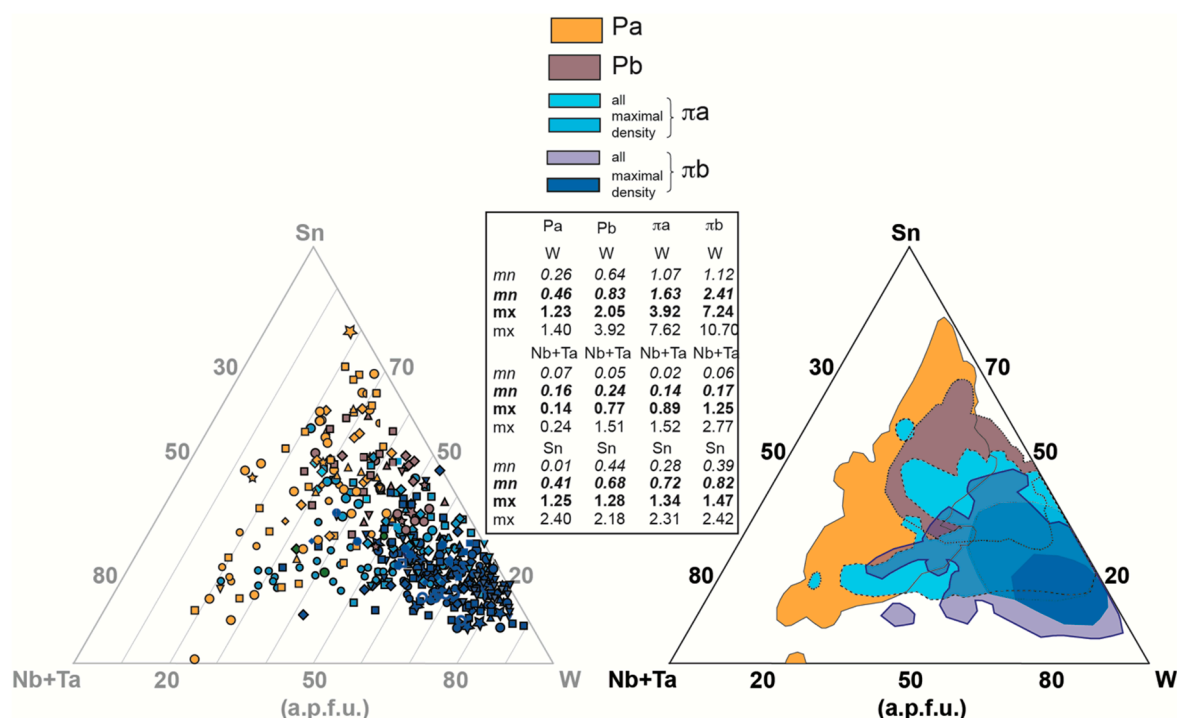


Figure 7. Demonstration of the sector zoning compositional effects in the W–Sn–(Nb + Ta) triangular diagram. Insert: minimal and maximal values (wt %) for W, Nb + Ta and W according to the type of faces. Both absolute (*italics*) and average (**bold**) values are given. Note the regular changes from the less to the more efficient faces.

5.3. Compositional Zoning: Oscillatory Zoning

Superimposed to sector zoning, oscillatory zoning is conspicuous, in particular in the pyramid sections (π_a and π_b). In most of the large crystals from Qcs veinlets, and in many of the smaller crystals in the wall rocks, oscillatory zoning is characterized by alternation of “clear” and “dark” bands in BSE images (Figure 8). Zoning characteristics are the same regardless of the rutile setting. The band boundaries appear as clear-cut, although in many instances the boundary is marked by a short-range but continuous variation of the grey hues, from the clear to the dark band. In the latter case, it thus appears that the two bands form a doublet, limited by abrupt boundaries. In a limited number of occurrences, the doublet is inverted, starting from the dark band (Figure 8A).

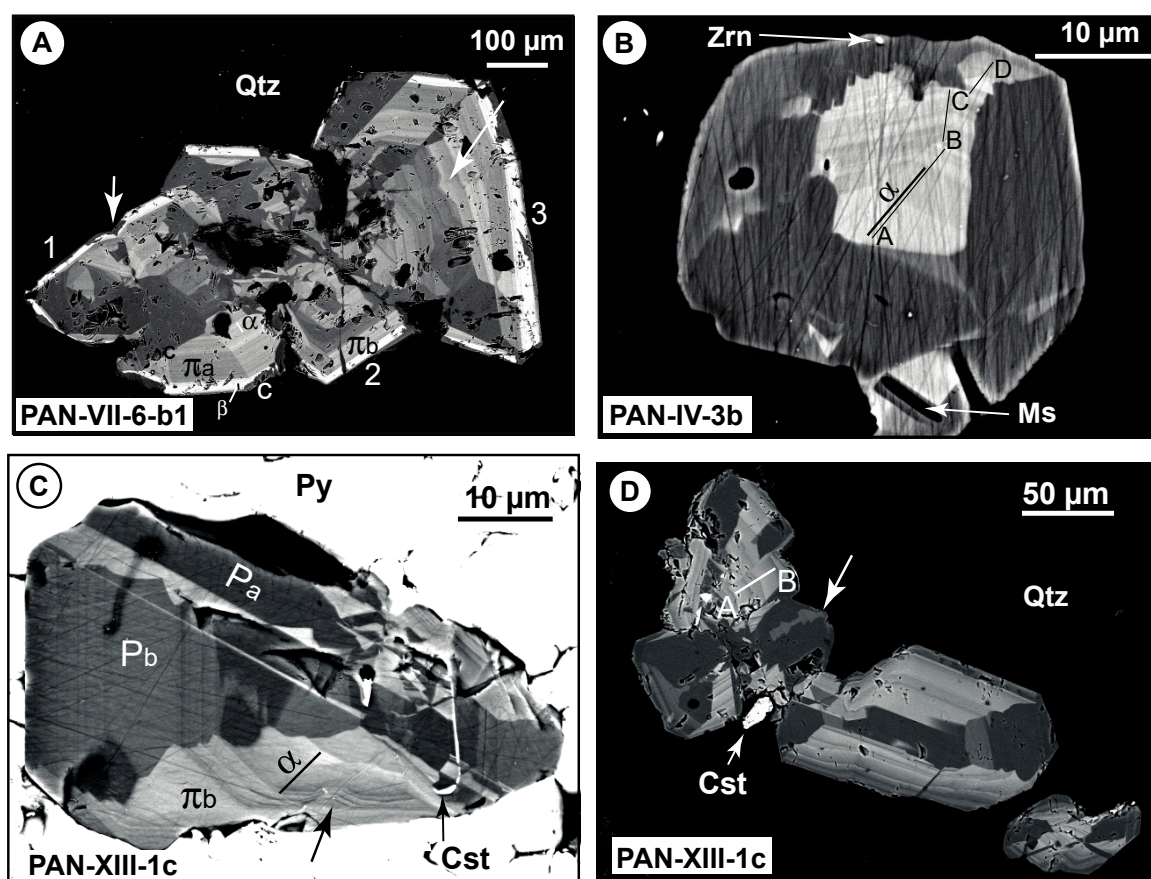


Figure 8. Rutile crystals with well-organized oscillatory zoning, in which are implanted the profiles of Figures 9 and 10 (SEM-BSE). (A) Three aggregated large crystals (1, 2, 3) from a Qcs veinlet. Profiles α and β in Figure 9 are from crystal 1. The two dipyrramids (π_a and π_b) are well displayed. Note the late corrosion (c) and the presence of twins (arrows, cf. Figure 3A). (B) Small crystal from a tourmalinized wall rock. Profile α is presented in Figure 9, and profile ABCD in Figure 10. Zrn zircon (C) Large crystal from a Qcs veinlet that we named Rt 5. The crystal is encapsulated in a late pyrite (Py), and crosscut by cassiterite (Cst). Note the convoluted oscillatory zoning (arrow). Profile α is presented in Figure 9. (D) Group of crystals from the same Qcs veinlet. Note the well expressed "fir-tree" texture (arrow). Profile AB is presented in Figure 10 where is noted as Rt7. Cst cassiterite.

Careful examination at high resolution suggests that doublets may in reality be the rule, the transition between the clear and dark bands being however extremely fast, in the micrometer range. The size of the bands is highly variable, in the 10–25 μm range (with possible intercalations of smaller 1–5 μm ribbons) in the larger crystals, down to 1–5 μm in the smaller crystals from the wall rocks (e.g., Figures 3C and 8B). At the crystal scale, zoning is expressed as succession of large strips, in the 50–150 μm range in the larger crystals, and 5–15 μm in the smaller. Each strip groups several elementary bands or doublets. The strips are characterized by major compositional changes as revealed in both SEM imaging and X-ray (EPMA) mapping (Figure 6).

All the minor elements, W, Nb + Ta, Fe, V, Cr and Sn, are involved in the compositional zoning. Three zoning scales must be considered. (i) At the band scale, owing to their small size, only in a very limited number of cases was construction of a profile possible. The results (Figure 9) did not provide a systematic organisation of the data. (ii) At the doublet scale (Figures 9 and 10) it appears that the clear bands are in general enriched in W relatively to the dark ones, whereas the inverse is true for Nb and Ta, which are most commonly conspicuously enriched in the latter. The clear/dark sharp boundary is always well reflected into jumps in these minor element contents. Tin and vanadium behavior is more

erratic, these elements being either correlated or anti-correlated with Nb and Ta. (iii) At the crystal scale, some regularity is observed.

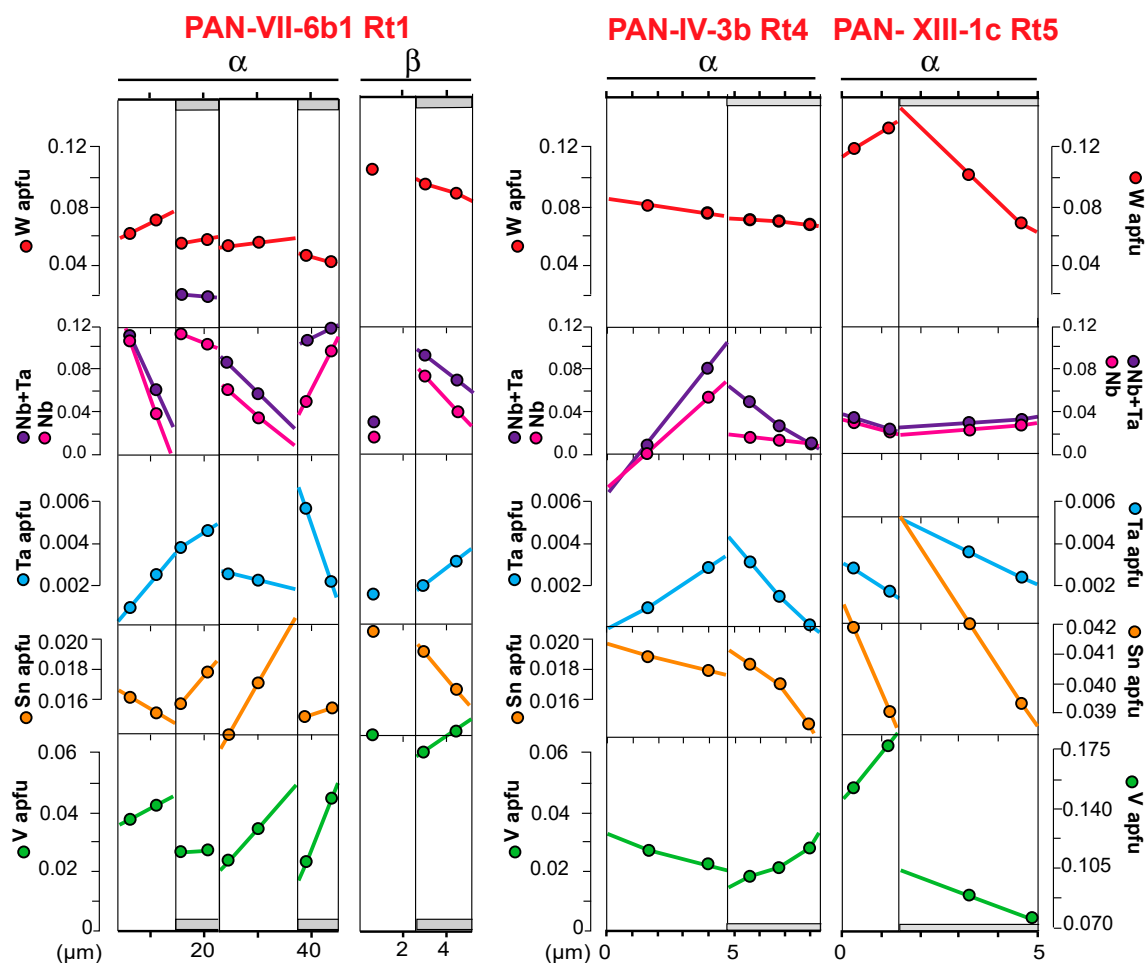


Figure 9. A selection of doublet profiles. The profiles are located in Figure 8 (PAN-VII-6-b1: Figure 8A; PAN-IV-3b: Figure 8B; PAN-XIII-1c: Figure 8C). Explanations in the text.

As seen in Figures 4 and 10, there is a clear tendency of Nb to be anti-correlated with W, and element contents are modulated at the scale of a few doublets (Figure 10). Tin and vanadium are less variable, and display contradictory behavior, being either correlated with Nb + Ta and anti-correlated with W (Figure 4J–M) or the contrary (Figure 4B–D and Figure 4F–H), just as in the doublet cases. Comparison of rutile crystals from different settings, even at the sample scale, shows that there are no general correlations: crystals may exhibit evolution from a Nb-rich and W-poor core to a W-rich and Nb-poor rim (PAN-VII-6-b1, Figure 4K,L), or the inverse (Figure 4F,G), or show moderate variations around middle W contents, which seems the most common case (Figure 4C).

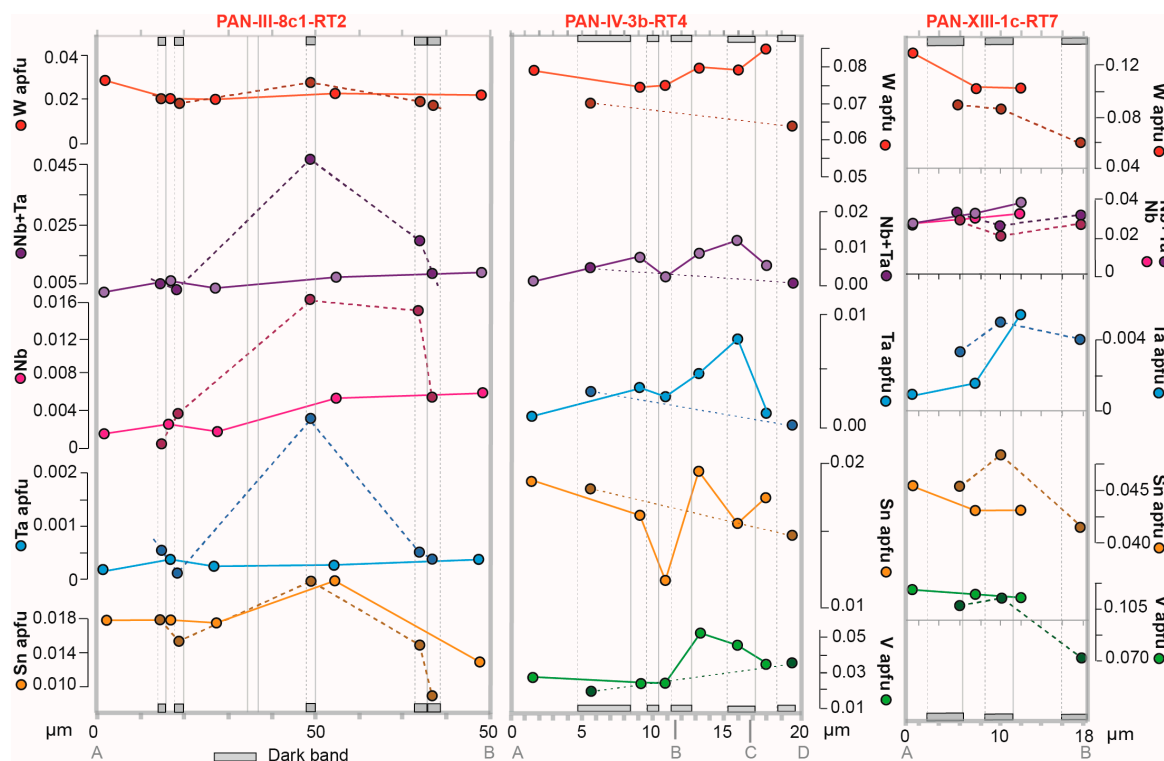


Figure 10. Minor element profiles in a selection of doublets from Panasqueira rutile, showing the time-controlled modulation of the minor element contents. Continuous tie-lines rely the onset of clear bands, whereas dotted tie-lines rely the onset of dark bands. The profiles are located in Figure 3 (PAN-III-8-c1-Rt2: Figure 3E, line AB) and in Figure 8 (PAN-IV-3b-Rt4: Figure 8B, line ABCD; PAN-XIII-1c-Rt7: Figure 8D, line AB). Explanations in the text.

6. Discussion

6.1. Oscillatory Zoning: External or Internal Control?

Several theoretical and experimental works, concerning either silicate growth in a magmatic medium [69–72], or the hydrothermal growth of barite [73], or calcite [74,75], have shown that oscillatory zoning may be due to internal factors. The competition between the growth speed and the elemental diffusion rates leads, in some conditions, to a self-organized process resulting in oscillatory zoning (OZ) without need for a change in the generating medium. Some workers emphasize the role of “impurities” in the appearance of self-organization, e.g., [76,77]. The self-organization point of view has been however challenged, some workers pointing out that oscillatory zoning may be related to both internal and external factors, e.g., [6], and others showing that oscillatory zoning may be entirely controlled by external factors, e.g., [78,79]. Experiments on calcite growth lead [75] to conclude that whereas large scale elemental variations reflect the overall changes of the growth solution, the finer scale modulations (OZ) are caused by growth-rate controlled incorporation of trace elements.

All the self-organization models yield stationary theoretical profiles characterized by more or less pronounced asymmetry, quasi-periodical evolution of the composition, regular size of the bands with oscillation between constant bounds. Nevertheless, very strong gradients may be produced, mimicking discontinuities. These characteristics are poorly matched by the doublets characterizing OZ in the Panasqueira rutile crystals (Figure 8): (i) the successive doublets are of various size, (ii) there is no real oscillation of the contents between fixed bounds from one doublet to the other, (iii) the internal structure of the doublets is not regular, the clear and dark bands being variously large or narrow between adjacent doublets (Figure 9), and (iv) elemental variations within doublets are not constrained to one and the same pattern. Therefore, to the possible exception of the narrower banding in the large

crystals (which could well be explained by self-organization), it must be concluded that the oscillatory zoning in the Panasqueira rutile crystals was essentially developed under external constraints. As crystallization temperature is not expected to have much varied [63], and unless pressure variations exert a major control on element partitioning into the rutile, which is thought to be unlikely, it results that the zoning reflects variations in the composition of the hydrothermal fluid.

Owing to sector zoning, interpretation must be based on homogeneous data, i.e., on data from the same kind of crystal forms, namely on the pyramid data, in particular, from the π_b faces. With this restriction, the rutile data may help to further enlighten the fluid characteristics. Yet, the information the rutile can yield must be considered to cover shorter time ranges than in the tourmaline case. This is shown by the absence of global correlation in the zoning features, suggesting that the crystallization of a given rutile crystal spanned less time than the coeval tourmaline. This is consistent with the fact that well-zoned rutile crystals may be included in tourmaline.

6.2. Open or Closed System Evolution?

Compositional variations may be controlled by either close- or open-system conditions of growth. There are no experimental data to constrain the W behavior in the course of fractional crystallization of a W-bearing rutile. According to [80], Nb being more compatible than Ta in a rutile crystal, a decrease of the Nb to Nb + Ta ratio is expected during crystallization of a Nb–Ta rutile in a closed system. As seen in Figure 9, a decrease of this ratio is not systematic, and when occurring, it is not associated with a correlative systematic variation of neither W nor Nb + Ta contents. In addition, the strong compositional changes at the clear/dark boundary in the OZ doublets is difficult to reconcile with fractional crystallization, which is on the contrary expected to yield rather continuous compositional variations. It is thus thought that the Panasqueira rutile grew under open-system conditions. Yet, in the context of sector zoning, it must be recalled that, according to [68], within-sector compositional changes may be induced by simply changing the normal growth rates of the corresponding faces, these changes being however difficult to separate from those in fluid chemistry. In the present case, it is thought that this effect may in part explain the apparently chaotic aspects of the minor elements behavior in the profiles of Figure 10. In an open-system perspective, most of the doublets may be viewed as the result of the successive influx of (i) a W-rich, Nb–Ta poor fluid, abruptly replaced by (or mixed to) (ii) a Nb–Ta-rich and W-poor fluid.

6.3. Oscillatory Zoning as a Consequence of Seismic Activity?

To go further in the interpretation, we must now consider the timescale of growth for a given doublet. For a large spectrum of mineral species, and in a large temperature (25–450 °C) and pressure (0.1–200 MPa) range, experimentally measured crystal growth rates are comprised between a few 10^{-1} nm·s⁻¹ and 10–20 (up to 100) nm·s⁻¹ (ZnO [81]; berlinite [82]; quartz [83,84]; fluorite and AgCl [85]; vaterite [86]; calcite [87–89]). As a rule, the rates increase with the concentration of the solution and the temperature of crystallization. For the Panasqueira rutile, growing at c. 450 °C, it seems then reasonable to bracket the growth rates between 1 and 10 nm·s⁻¹, as a first order of magnitude. With such values, the time growth of a 20 µm-large band in a rutile crystal would be in the order of 2×10^3 to 2×10^5 s, i.e., from less than 1 h to ~2 days, meaning that it should be also the time scale for the turning over the flow feeding at the doublet growth scale. This, in turn, is reminiscent of seismically controlled fluid flow processes. It has been shown that seismic events have the capacity to activate micro-permeability in the affected rock volume, allowing the incorporation of otherwise captive fluids in the circulating fluid flow [90,91]. The time constant of the process is in the order of a few hours to a few days, consistent with the estimated growth rates for the rutile. An experimental work on apatite [92] confirms that complex zoning patterns may result from short-lived fluid flow events associated with rapid fluid composition fluctuations such as those occurring during a seismic cycle. Thus, the formation of a doublet could be understood as the result of seismic activity. A (micro) seismic event would allow in a first time the influx in the growing environment of the main fluid circulating at

this time at the deposit scale, and a light band would grow. After a short time lag, a new fluid, coming from a low permeability reservoir, would in turn invade the growing environment, triggering the growth of the succeeding dark band.

6.4. Nature of the Fluid(s)

At Panasqueira, the early tourmalinization process is demonstrated to result from the progressive mixing between a first fluid F1, characterized by a Co–Cu–Pb–Sc–Sr–V–Cr–Sn–Nb–Ta elemental assemblage, and a second fluid F2, characterized by the F–Li–Fe–Mn–Zn–W elemental assemblage [65]. Both fluids are thought to be of metamorphic origin. At the end of the tourmaline growth, when rutile is crystallizing, F2 is dominant in the mineralizing mixed fluid. This is in agreement with the composition of the clear bands in the rutile doublets, which are characterized by high W contents. It is by contrast impossible to relate to F1 nor to F2 the repetitive infiltrations of a small quantity of fluid during micro-seismic events that are thought to be at the origin of the dark bands. It cannot be F1, owing to the lack of systematic positive correlation between Nb + Ta and V or Sn in these dark bands. In addition, neither in F1 nor in F2 is observed the high Nb to W ratio found in the dark bands. Consequently, a third fluid F3 seems to be recorded in the rutile growth, and rutile thus appears as a very sensitive marker of fluid evolution.

There is a rare metal granite (RMG) layer atop of the Panasqueira granite (Figure 1B), and these RMG are characterized by abundant Nb-rich columbo-tantalite (Nb/Nb + Ta in the 0.74–0.93 range). However, they are poor in cassiterite, a fact which is reflected in rather low Sn contents in the granites (≤ 75 ppm) [47]. It is thus tempting to relate fluid F3 to these Nb-rich granites. Nevertheless, F3 is unlikely to be a magmatic-hydrothermal fluid, because there is no evidence at the RMG-micaschist boundary for an interaction between the wall rock and a fluid issued from the granitic melt, except a limited Rb and Sr enrichment of micaschists on a few meters [47]. On the other hand, the RMG layer could well have acted as the low-permeability reservoir required by the model presented in the previous section. It may thus be proposed that at the favor of seismic events, the main F1/F2 mixture could invade the RMG. During the inter-seismic period of retention, high temperature fluid-rock interaction could cause the F1/F2 mixture to evolve into fluid F3. The latter would be released at the occasion of the next seismic event, causing the growth of a new dark band in the rutile, whereas coeval invasion of F1/F2 into the granite would initiate the following cycle.

7. Conclusions

1. From the crystal-chemistry point of view, iron and vanadium in the Panasqueira rutile crystals are predominantly present as Fe^{3+} and V^{4+} , respectively.

2. The conspicuous sector zoning is due to differential incorporation of minor elements onto pyramidal and prismatic faces, the latter being by far less efficient. Two families of both types are involved, but could not be indexed. W is more strongly incorporated than Nb + Ta onto the more efficient faces, whereas Sn and V contents are nearly not impacted. The net effect of the sector zoning is thus a progressive increase of the relative weight of Sn from the most efficient pyramid family to the less efficient prism family of faces, somewhat in combination with a less significant increase of the relative weight of Nb + Ta.

3. The Panasqueira rutile rank among the richest in tungsten worldwide (up to 10.7 wt % W). This is connected with this rutile heralding the main wolframite deposition event.

4. The conspicuous oscillatory zoning concerns most minor elements: W, Nb + Ta, Fe, V, Cr and Sn. It does not result from a self-organizing process, and records open-system conditions of crystallization. The doublets of “clear” and “dark” bands that make the oscillatory zoning are viewed as the result of the successive influx of (i) a W-rich, Nb + Ta poor fluid, abruptly replaced by (or mixed to) (ii) a Nb-rich and W-poor fluid. Whereas the clear bands likely crystallized from the main fluid associated with the tourmaline growth, the dark bands are thought to record repetitive influxes of another fluid,

released from a tight reservoir in relation to seismic events. This reservoir was likely the rare metal granite layer atop of the Panasqueira granite.

5. Rutile appears to be a very sensitive marker of fluid evolution in hydrothermal systems, in the same way as rutile is a sensitive marker of melt evolution in magmatic systems.

Supplementary Materials: The following are available online at <http://www.mdpi.com/2075-163X/9/1/9/s1>, Table S1: SEM-EDS analyses of the Panasqueira rutile.

Author Contributions: Conceptualization, E.C., C.M. and M.C.; Methodology and Data Curation, A.L.; Validation, L.T. and F.P.; Writing—Original Draft Preparation, E.C.; Writing—Review & Editing, E.C. and C.M.

Funding: This work was funded by the ERAMIN project NewOres financed by ANR (ANR-14-EMIN-0001), and Labex Ressources 21 (supported by the French National Research Agency through the national program “Investissements d’avenir”) with reference ANR-10-LABX 21-LABEX RESSOURCES 21. LA-ICP-MS equipment was financed by CPER program (National Funds–Lorraine region–FEDER).

Acknowledgments: This work benefited from the analytical capabilities of the GeoRessources Laboratory (Université de Lorraine, CNRS, CREGU), and the authors gratefully acknowledge Olivier Rouer and Lise Salsi for their technical help. We thank Isabella Pignatelli for her assistance in crystallographic approaches. We are most grateful to Beralto Tin and Wolfram S.A. for permitting access to the Panasqueira underground mine. Three anonymous reviewers are warmly thanked for their constructive criticism and help in improving the manuscript.

Conflicts of Interest: The authors declare no conflict of interest.

References

- Meinhold, G. Rutile and its applications in earth sciences. *Earth-Sci. Rev.* **2010**, *102*, 1–28. [CrossRef]
- Graham, J.; Morris, R.C. Tungsten- and antimony-substituted rutile. *Mineral. Mag.* **1973**, *39*, 470–473. [CrossRef]
- Hassan, W.F. Geochemistry and mineralogy of Ta–Nb rutile from Peninsular Malaysia. *J. Asian Earth Sci.* **1994**, *10*, 11–23. [CrossRef]
- Murad, E.; Cashion, J.D.; Noble, C.J.; Pilbrow, J.R. The chemical state of Fe in rutile from an albitite in Norway. *Mineral. Mag.* **1995**, *59*, 557–560. [CrossRef]
- Smith, D.; Perseil, E.-A. Sb-rich rutile in the manganese concentrations at St. Marcel-Praborna, Aosta Valley, Italy; petrology and crystal-chemistry. *Mineral. Mag.* **1997**, *61*, 655–669. [CrossRef]
- Rice, C.; Darke, K.; Still, J. Tungsten-bearing rutile from the Kori Kollo gold mine Bolivia. *Mineral. Mag.* **1998**, *62*, 421–429. [CrossRef]
- Zack, T.; Kronz, A.; Foley, S.F.; Rivers, T. Trace element abundances in rutiles from eclogites and associated garnet mica schists. *Chem. Geol.* **2002**, *184*, 97–122. [CrossRef]
- Bromiley, G.D.; Hilairt, N. Hydrogen and minor element incorporation in synthetic rutile. *Mineral. Mag.* **2005**, *69*, 345–358. [CrossRef]
- Scott, K.M. Rutile geochemistry as a guide to porphyry Cu–Au mineralization, Northparkes, New South Wales, Australia. *Geochem. Explor. Environ. Anal.* **2005**, *5*, 247–253. [CrossRef]
- Carruzzo, S.; Clarke, D.B.; Pelrine, K.M.; MacDonald, M.A. Texture, composition, and origin of rutile in the South Mountain Batholith, Nova Scotia. *Can. Mineral.* **2006**, *44*, 715–729. [CrossRef]
- Zack, T.; von Eynatten, H.; Kronz, A. Rutile geochemistry and its potential use in quantitative provenance studies. *Sediment. Geol.* **2004**, *171*, 37–58. [CrossRef]
- Triebold, S.; von Eynatten, H.; Luvizotto, G.L.; Zack, T. Deducing source rock lithology from detrital rutile geochemistry: An example from the Erzgebirge, Germany. *Chem. Geol.* **2007**, *244*, 421–436. [CrossRef]
- Plank, T.; Langmuir, C.H. The geochemical composition of subducting sediment and its consequences for the crust and mantle. *Chem. Geol.* **1998**, *145*, 325–394. [CrossRef]
- La Tourette, T.; Hervig, R.L.; Holloway, J.R. Trace element partitioning between amphibole, phlogopite and basanite melt. *Earth Planet. Sci. Lett.* **1995**, *135*, 13–30. [CrossRef]
- Barth, M.G.; McDonough, W.F.; Rudnick, R.L. Tracking the budget of Nb and Ta in the continental crust. *Chem. Geol.* **2000**, *165*, 197–213. [CrossRef]
- Zack, T.; Stockli, D.F.; Luvizotto, G.L.; Barth, M.G.; Belousova, E.; Wolfe, M.R.; Hinton, R.W. In situ U–Pb rutile dating by LA-ICP-MS: ^{208}Pb correction and prospects for geological applications. *Contrib. Mineral. Petrol.* **2011**, *162*, 515–530. [CrossRef]

17. Ferreira-Filho, C.F.; Naldrett, A.J.; Fuck, R.A.; Kamo, S.L.; Krogh, T.E. Zircon and rutile U-Pb geochronology of the Niquelândia layered mafic and ultramafic intrusion, Brazil: Constraints for the timing of magmatism and high grade metamorphism. *Prec. Res.* **1994**, *68*, 241–255. [\[CrossRef\]](#)
18. Richards, J.P.; Krogh, T.E.; Spooner, E.T.C. Fluid inclusion characteristics and U–Pb rutile age of late hydrothermal alteration and veining at the Musoshi stratiform copper deposit, Central African copper belt, Zaire. *Econ. Geol.* **1998**, *83*, 118–139. [\[CrossRef\]](#)
19. Schandl, E.S.; Davis, D.W.; Krogh, T.E. Are the alteration halos of massive sulfide deposits syngenetic? Evidence from U–Pb dating of hydrothermal rutile at the Kidd volcanic center, Abitibi subprovince, Canada. *Geology* **1990**, *18*, 505–508. [\[CrossRef\]](#)
20. Wong, L.; Davis, D.W.; Krogh, T.E.; Robert, F. U–Pb zircon and rutile geochronology of Archean greenstone formation and gold mineralization in the Val d’Or region, Quebec. *Earth Planet. Sci. Lett.* **1991**, *104*, 325–336. [\[CrossRef\]](#)
21. Carocci, E.; Marignac, C.; Cathelineau, M.; Truche, L.; Pinto, F. Trace Elements in Tourmaline: Markers of Incipient W Deposition in Panasqueira Mine. In Proceedings of the Goldschmidt Conference, Paris, France, 13–18 August 2017.
22. Zack, T.; Moraes, R.; Kronz, A. Temperature dependence of Zr in rutile: Empirical calibration of a rutile thermometer. *Contrib. Mineral. Petrol.* **2004**, *148*, 471–488. [\[CrossRef\]](#)
23. Novák, M.; Černý, P. Niobium–tantalum oxide minerals from complex granitic pegmatites in the Moldanubicum, Czech Republic: Primary versus secondary compositional trends. *Can. Mineral.* **1998**, *36*, 659–672.
24. Tindle, A.G.; Breaks, F.W. Oxide minerals of the Separation Rapids rare-element granitic pegmatite group, Northwestern Ontario. *Can. Mineral.* **1998**, *36*, 609–635.
25. Černý, P.; Goad, B.E.; Hawthorne, F.C.; Chapman, R. Fractionation trends of the Nb- and Ta-bearing oxide minerals in the Greer Lake pegmatitic granite and its pegmatite aureole, southeastern Manitoba. *Am. Mineral.* **1986**, *71*, 501–517.
26. Černý, P.; Chapman, R.; Simmons, W.B.; Chackowsky, L.E. Niobian rutile from the McGuire granitic pegmatite, Park County, Colorado; solid solution, exsolution, and oxidation. *Am. Mineral.* **1999**, *84*, 754–763. [\[CrossRef\]](#)
27. Hanson, S.L.; Simmons, W.B.; Falster, A.U. Nb–Ta–Ti oxides in granitic pegmatites from the Topsham pegmatite district, southern Maine. *Can. Mineral.* **1998**, *36*, 601–608.
28. Uher, P.; Černý, P.; Chapman, R.; Határ, J.; Miko, O. Evolution of Nb, Ta-oxide minerals in the Prašivá granitic pegmatites, Slovakia. I. Primary Fe, Ti-rich assemblage. *Can. Mineral.* **1998**, *36*, 525–534.
29. Belkasm, M.; Cuney, M.; Pollard, P.J.; Bastoul, A. Chemistry of the Ta-Nb-Sn-W oxide minerals from the Yichun rare metal granite (SE China): Genetic implications and comparison with Moroccan and French Hercynian examples. *Mineral. Mag.* **2000**, *64*. [\[CrossRef\]](#)
30. Aurisicchio, C.; De Vito, C.; Ferrini, V.; Orlandi, P. Nb and Ta oxide minerals in the Fonte Del Prete granitic pegmatite dike, Island of Elba, Italy. *Can. Mineral.* **2002**, *40*, 799–814. [\[CrossRef\]](#)
31. Bouabsa, L.; Marignac, C.; Chabbi, R.; Cuney, M. 2010. The Filfila (NE Algeria) topaz bearing granites and their rare metal minerals: Petrologic and metallogenic implications. *J. Afr. Earth Sci.* **2010**, *56*, 107–113. [\[CrossRef\]](#)
32. Rabbia, O.M.; Hernández, L.B. Mineral chemistry and potential applications of natural-multi-doped hydrothermal rutile from porphyry copper deposits. In *Rutile: Properties, Synthesis and Application*; Low, I.-M., Ed.; Nova Science Publishers, Inc.: Hauppauge, NY, USA, 2012; pp. 209–228.
33. Clark, J.R.; Williams-Jones, A.E. *Rutile as a Potential Indicator Mineral for Metamorphosed Metallic ore Minerals Deposits*; Rapport Final de DIVEX, Sous-projet SC2; Divex: Montréal, QC, Canada, 2004; 17p.
34. Scott, K.M.; Radford, N.W. Rutile compositions at the Big Bell Au deposit as a guide for exploration. *Geochem. Explor. Environ. Anal.* **2007**, *7*, 353–361. [\[CrossRef\]](#)
35. Dostal, J.; Kontak, D.J.; Chatterjee, A. Trace element geochemistry of scheelite and rutile from metatubidite-hosted quartz vein gold deposits, Meguma Terrane, Nova Scotia, Canada: Genetic implications. *Mineral. Petrol.* **2009**, *97*, 95–109. [\[CrossRef\]](#)
36. Scott, K.M.; Radford, N.; Hough, R.; Reddy, S. Rutile compositions in the Kalgoorlie Goldfields and their implications for exploration. *Aust. J. Earth Sci.* **2011**, *58*, 803–812. [\[CrossRef\]](#)

37. Černý, P.; Novák, M.; Chapman, R.; Ferreira, K.J. Subsolidus behavior of niobian rutile from the Písek region, Czech Republic: A model for exsolution in W- and $\text{Fe}^{2+} \gg \text{Fe}^{3+}$ -rich phases. *J. Geosci.* **2007**, *52*, 143–159. [CrossRef]
38. Harlaux, M. Tungsten and Rare-Metal (Nb, Ta, Sn) Hydrothermal Metallogenic Systems in the Late Variscan Orogenic Context: Example of the French Massif Central. Ph.D. Thesis, Lorraine University, Lorraine, France, 2016; p. 576.
39. Michailidis, K.M. An EPMA and SEM study of niobian-tungstenian rutile from the Fanos aplitic granite, central Macedonia, northern Greece. *Neues Jahrbuch für Mineralogie-Monatshefte* **1997**, *12*, 549–563.
40. Baksheev, T.A.; Guseva, E.V.; Spiridonov, E.M. W- rutile from vein post-skarn mineralization of the Bestiube deposit, north Kazakhstan. In Proceedings of the 16th General Meeting Abstracts International Mineralogical Association (IMA), Pisa, Italy, 4–9 September 1994; Volume 16, pp. 25–26.
41. Vigne, J.-L.; André, G.; Kapal, F. Données industrielles, économiques, géographiques sur les principaux produits chimiques, métaux, matériaux, 2018. Available online: <http://www.societechimiquedefrance.fr/extras/Donnees/acc.htm> (accessed on 20 December 2018).
42. Almonty Industries. Report NI 43-101. Technical Report on the Mineral Resources and Reserves of the Panasqueira Mine, Portugal. 2016. Available online: http://www.almonty.com/_resources/Panasqueira_43-101_Tech_Rep_Dec16_SEDAR.PDF (accessed on 20 December 2018).
43. Díez Fernández, R.; Barreiro, J.G.; Martínez Catalán, J.R.; Ayarza, P. Crustal thickening and attenuation as revealed by regional fold interference patterns: Ciudad Rodrigo basement area (Salamanca, Spain). *J. Struct. Geol.* **2013**, *46*, 115–128. [CrossRef]
44. Ribeiro, R.F. Gravimetric Modelling and Geological Interpretation of Argemela-Panasqueira Area. Ph.D. Thesis, Porto University, Porto, Portugal, 2017; p. 61.
45. Kelly, W.C.; Rye, R.O. Geologic, fluid inclusion, and stable isotope studies of the tin–tungsten deposits of Panasqueira, Portugal. *Econ. Geol.* **1979**, *74*, 1721–1822. [CrossRef]
46. Bussink, R.W. Geochemistry of the Panasqueira tungsten-tin deposit, Portugal. *Geol. Ultraiect.* **1984**, *33*, 1–159.
47. De Amorin, A. Petrographie géochimie des granitoides de la mine de W de Panasqueira (Portugal): Rôle dans la genèse des minéralisations. Unpublished MSc Thesis, Lorraine University (France), Lorraine, France, 2017; p. 31.
48. Thadeu, D. Geologia e jazigos de chumbo e zinco da Beira Baixa. *Bol. da SGP (Soc. Geol. de Por.)* **1951**, *9*, 1–144.
49. Polya, D.A. Chemical behaviour of tungsten in hydrothermal fluids and genesis of the Panasqueira W-Cu-Sn deposit, Portugal. Unpublished Ph.D. Thesis, Manchester University, Manchester, UK, 1988.
50. Polya, D.A. Compositional variation in wolframites from the Barroca Grande mine, Portugal: Evidence for fault-controlled ore formation. *Mineral. Mag.* **1988**, *52*, 497–503. [CrossRef]
51. Polya, D.A. Efficiency of hydrothermal ore formation and the Panasqueira W-Cu(Ag)-Sn vein deposit. *Nature* **1988**, *333*, 838–841. [CrossRef]
52. Polya, D.A. Chemistry of the main-stage ore-forming fluids of the Panasqueira W-Cu(Ag)-Sn deposit, Portugal: Implications for models of ore genesis. *Econ. Geol.* **1989**, *84*, 1134–1152. [CrossRef]
53. Snee, L.W.; Sutter, J.F.; Kelly, W.C. Thermochronology of economic mineral deposits: Dating the stages of mineralisation at Panasqueira, Portugal, by high-precision ^{40}Ar - ^{39}Ar age spectrum techniques on muscovite. *Econ. Geol.* **1988**, *83*, 335–354. [CrossRef]
54. Noronha, F.; Dória, F.; Dubessy, J.; Charoy, B. Characterization and timing of the different types of fluids present in the barren and ore veins of the W-Sn deposit of Panasqueira, central Portugal. *Miner. Depos.* **1992**, *27*, 72–79. [CrossRef]
55. Lüders, V. Contribution of infrared microscopy to fluid inclusion studies in some opaque minerals (wolframite, stibnite, bournonite): Metallogenic implications. *Econ. Geol.* **1996**, *91*, 1462–1468. [CrossRef]
56. Foxford, K.A.; Nicholson, R.; Polya, D.A. Textural evolution of W-Cu-Sn bearing hydrothermal quartz veins at Minas da Panasqueira, Portugal. *Mineral. Mag.* **1991**, *55*, 435–445. [CrossRef]
57. Foxford, K.A.; Nicholson, R.; Polya, D.A.; Hebblethwaite, R.P.B. Extensional failure and hydraulic valving at Minas da Panasqueira, Portugal: Evidence from vein spatial distributions, displacements and geometries. *J. Struct. Geol.* **2000**, *22*, 1065–1086. [CrossRef]

58. Polyá, D.A.; Foxford, K.A.; Stuart, F.; Boyce, A.; Fallick, A.E. Evolution and paragenetic context of low δD hydrothermal fluids from the Panasqueira W-Sn deposit, Portugal: New evidence from microthermometric, stable isotope, noble gas and halogen analyses of primary fluid inclusions. *Geochim. Cosmochim. Acta* **2000**, *64*, 3357–3371. [[CrossRef](#)]
59. Lourenço, A. Paleofluidos e mineralizações associadas às fases tardias da Orogenia Hercínica. Unpublished Ph.D. Thesis, Porto University, Porto, Portugal, 2002.
60. Burnard, P.G.; Polyá, D.A. Importance of mantle derived fluids during granite associated hydrothermal circulation: He and Ar isotopes of ore minerals from Panasqueira. *Geochim. Cosmochim. Acta* **2004**, *68*, 1607–1615. [[CrossRef](#)]
61. Pinto, F.; Vieira, R.; Noronha, F. Different cassiterite generations at the Panasqueira Deposit (Portugal): Implications for the metal zonation model. In *Mineral Resources in a Sustainable World*; André-Mayer, A.S., Cathelineau, M., Muchez, P., Pirard, E., Sindern, S., Eds.; Proceedings of the Society of Geology Applied to Mineral Deposits (SGA) Biennial Meeting: Nancy, France, 2015; Volume 2, pp. 827–830.
62. Lecumberri-Sanchez, P.; Vieira, R.; Heinrich, C.; Pinto, F.; Walle, M. Fluid-rock interaction is decisive for the formation of tungsten deposits. *Geology* **2017**, *45*, 579–582. [[CrossRef](#)]
63. Codeço, M.S.; Weis, P.; Trumbull, R.B.; Pinto, F.; Lecumberri-Sanchez, P.; Wilke, F.D. Chemical and boron isotopic composition of hydrothermal tourmaline from the Panasqueira W-Sn-Cu deposit, Portugal. *Chem. Geol.* **2017**, *468*, 1–16. [[CrossRef](#)]
64. Launay, G.; Sizaret, S.; Guillou-Frottier, L.; Gloaguen, E.; Pinto, F. Deciphering fluid flow at the magmatic-hydrothermal transition: A case study from the world-class Panasqueira W-Sn-(Cu) ore deposit (Portugal). *Earth Planet. Sci. Lett.* **2018**, *499*, 1–12. [[CrossRef](#)]
65. Carocci, E.; Marignac, C.; Cathelineau, M.; Pinto, F.; Truche, L. Le stade initial du dépôt de la wolframite dans le gisement à W-Sn-Cu de Panasqueira (Portugal): Caractérisation indirecte des fluides par l'étude des tourmalines précoces. In Proceedings of the 24th Réunion des Sciences de la Terre, Lille, France, 22–26 October 2018; p. 439.
66. Černý, P.; Ercit, T.S. Mineralogy of niobium and tantalum: crystal chemical relationships, paragenetic aspects and their economic implications. In *Lanthanides, Tantalum and Niobium*; Möller, P., Černý, P., Saupé, F., Eds.; Springer-Verlag: Heidelberg, Germany, 1989; pp. 27–79.
67. Liu, L.; Xiao, Y.; Aulbach, S.; Li, D.; Hou, Z. Vanadium and niobium behavior in rutile as a function of oxygen fugacity: Evidence from natural samples. *Contrib. Mineral. Petrol.* **2014**, *167*, 1025–1077. [[CrossRef](#)]
68. Paterson, B.A.; Stephens, W.E. Kinetically induced compositional zoning in titanite: Implications for accessory-phase/melt partitioning of trace elements. *Contrib. Mineral. Petrol.* **1992**, *109*, 373–385. [[CrossRef](#)]
69. Allègre, C.J.; Provost, A.; Jaupart, C. Oscillatory zoning: A pathological case of crystal growth. *Nature* **1981**, *294*, 223–228. [[CrossRef](#)]
70. Ortoleva, P.; Merino, E.; Moore, C.; Chadam, J. Geochemical self-organization. I: Reaction-transport feedbacks and modeling approach. *Am. J. Sci.* **1987**, *287*, 979–1007. [[CrossRef](#)]
71. L'Heureux, I. Oscillatory zoning in crystal growth: A constitutional undercooling mechanism. *Phys. Rev. E* **1993**, *48*, 4460–4469. [[CrossRef](#)]
72. Miura, H.; Tsukamoto, K. Role of Impurity on Growth Hysteresis and Oscillatory Growth of Crystals. *Cryst. Growth Des.* **2013**, *13*, 3588–3595. [[CrossRef](#)]
73. Katsev, S.; L'Heureux, I. Autocatalytic model of oscillatory zoning in experimentally grown (Ba,Sr)SO₄ solid solution. *Phys. Rev. E* **2002**, *66*. [[CrossRef](#)]
74. Wang, Y.; Merino, E. Dynamic model of oscillatory zoning of trace elements in calcite: Double layer, inhibition, and self-organization. *Geochim. Cosmochim. Acta* **1992**, *56*, 587–596. [[CrossRef](#)]
75. Barker, S.L.L.; Cox, S.F. Oscillatory zoning and trace element incorporation in hydrothermal minerals: Insights from calcite growth experiments. *Geofluids* **2011**, *11*, 48–56. [[CrossRef](#)]
76. Guskov, S.S.; Faddeev, M.A.; Chuprunov, E.V. Concentration oscillations at doped crystal growth from solutions. *Crystallogr. Rep.* **2010**, *55*, 626–631. [[CrossRef](#)]
77. Shkutenberg, A.G.; Punin, Y.O. Micromorphological instability of a growing face as a source of oscillatory zoning in crystals. *Mineral. Mag.* **2011**, *75*, 169–183.
78. Ginibre, C.; Wörner, G.; Kronz, A. Minor and trace element zoning in plagioclase: Implications for magma chamber processes at Paríacota Volcano, N. Chile. *Contrib. Mineral. Petrol.* **2002**, *143*, 300–315. [[CrossRef](#)]

79. Ginibre, C.; Kronz, A.; Wörner, G. High-resolution quantitative imaging of plagioclase composition using accumulated back-scattered electron image: New constraints on oscillatory zoning. *Contrib. Mineral. Petrol.* **2002**, *142*, 436–448. [[CrossRef](#)]
80. Green, T.H.; Pearson, N.J. T-rich accessory phase saturation in hydrous mafic-felsic compositions at high P, T. *Chem. Geol.* **1986**, *54*, 185–201. [[CrossRef](#)]
81. Laudise, R.A.; Kolb, E.D.; Caporaso, A.J. Hydrothermal growth of large sound crystals of zinc oxide. *J. Am. Ceram. Soc.* **1964**, *47*. [[CrossRef](#)]
82. Kolb, E.D.; Grenier, J.-C.; Laudise, R.A. Solubility and growth of AlPO_4 in a hydrothermal solvent: HCl. *J. Cryst. Growth* **1981**, *51*, 178–182. [[CrossRef](#)]
83. Hosaka, M.; Taki, S. Hydrothermal growth of quartz crystals at low fillings in NaCl and KCl solutions. *J. Cryst. Growth* **1986**, *78*, 413–417. [[CrossRef](#)]
84. Lander, R.H.; Larese, R.E.; Bonnell, L.M. Toward more accurate quartz cement models: The importance of euhedral versus noneuhedral growth rates. *AAPG Bullet.* **2008**, *92*, 1537–1563. [[CrossRef](#)]
85. Nielsen, A.E.; Toft, J.M. Electrolyte crystal growth kinetics. *J. Cryst. Growth* **1984**, *67*, 278–288. [[CrossRef](#)]
86. Kralj, D.; Brecevic, L.; Nielsen, A.E. Vaterite growth and dissolution in aqueous solution I. Kinetics of crystal growth. *J. Cryst. Growth* **1990**, *104*, 793–800. [[CrossRef](#)]
87. Yanagisawa, K.; Feng, Q.; Ioku, N.; Yamasaki, N. Hydrothermal single crystal growth of calcite in ammonium acetate solution. *J. Cryst. Growth* **1996**, *163*, 285–294. [[CrossRef](#)]
88. Tai, C.Y.; Chien, W.-C.; Chen, C.-Y. Crystal growth kinetics of calcite in a dense fluidized-bed crystallizer. *AIChE J.* **1999**, *45*, 1605–1614. [[CrossRef](#)]
89. Teng, H.H.; Dove, P.M.; De Yoreo, J.J. Kinetics of calcite growth: Surface processes and relationships to macroscopic rate laws. *Geochim. Cosmochim. Acta* **2000**, *64*, 2255–2266. [[CrossRef](#)]
90. Charmoille, A. Traçage hydrochimique des interactions hydrauliques et mécaniques entre les volumes perméables et peu perméables au sein des aquifères fracturés carbonatés: Aquifère karstique de Fourbanne (Avant-pays jurassien, 25), Laboratoire naturel de Coaraze (Alpes Méridionales, 06). Ph.D. Thesis, Besançon University, Besançon, France, 2005.
91. Charmoille, A.; Fabbri, O.; Mudry, J.; Guglielmi, Y.; Bertrand, C. Post-seismic permeability change in a shallow fractured aquifer following a ML 5.1 earthquake (Fourbanne karst aquifer, Jura outermost thrust unit, eastern France). *Geophys. Res. Lett.* **2005**, *32*, LA8406. [[CrossRef](#)]
92. Borg, S.; Liu, W.; Pearce, M.; Cleverley, J.; MacRae, C. Complex mineral zoning patterns caused by ultra-local equilibrium at reaction interfaces. *Geology* **2014**, *42*, 415–418. [[CrossRef](#)]



© 2018 by the authors. Licensee MDPI, Basel, Switzerland. This article is an open access article distributed under the terms and conditions of the Creative Commons Attribution (CC BY) license (<http://creativecommons.org/licenses/by/4.0/>).